ADVANCED SUSTAINABLE SYSTEMS
www.advsustainsys.com

A Hierarchical Polyoxometalate/Pd/Mos_2 Hybrid: Developing an Efficient Novel Bifunctional Catalyst for Water Splitting

Melanie Guillen-Soler, Natalia V. Vassilyeva, Eugenia Pilar Quirós-Díez, Jose M. Vila-Fungueiriño, Alicia Forment-Aliaga, and Maria del Carmen Gimenez-Lopez**

Catalytic water splitting is a promising approach to produce clean hydrogen fuel from renewable energy sources. However, developing hybrid heterostructures capable of efficiently breaking down water into its constituent elements, hydrogen, and oxygen, presents a considerable challenge. In this study, a novel hierarchical POM/Pd/MoS_2 hybrid heterostructure, composed of sheets of MoS_2 modified with Pd nanoparticles and combined with a cobalt-based polyoxometalate (POM), serving as bifunctional catalyst for water splitting is reported. Through a synergistic synthetic approach, MoS_2, acting as a reducing agent, triggers the nucleation and growth of Pd nanoparticles, which, in turn, serve as anchoring sites for the polymerization of the cobalt-based POM into fibers. POM/Pd/MoS_2 hybrid exhibits an enhanced oxygen evolution reaction (OER) activity, comparable to the benchmark catalysts Ir/C and IrO_2/C in alkaline media, being its hydrogen evolution reaction (HER) activity similar to the activated Pd/MoS_2 hybrid. The intriguing electrocatalytic capability of the resulting material for producing hydrogen and oxygen through electrochemical means arises from the enhanced charge storage capacity and conductivity of MoS_2, the multi-electron transfer facilitated by the POM, and the high electrocatalytic activity of the metals.

1. Introduction

To achieve efficient conversion of renewable energy sources through water splitting, low-cost, earth-abundant, and robust electrocatalysts for oxygen evolution reaction (OER) and hydrogen evolution reaction (HER) are required. Transition metal sulfides,[1] nitrides,[2] carbides,[3] phosphides,[4] selenides,[5] borides, and metal-carbon hybrids have been applied for the HER,[6] whilst metal oxides, hydroxides, phosphates, and nanocomposites are demonstrated to be effective toward the OER.[7] Among these, metal sulfides electrocatalyst materials, (i.e., MoS_2, Ni_2S_3, CoS_2, and WS_2) have been reported to simultaneously catalyze OER and HER in alkaline electrolyte solutions and are proven to be cheaper alternatives for sustainable large-scale applications, compared to noble metals.[8] Specifically, molybdenum disulfide (MoS_2)-based materials are generally known as active electrocatalysts for the HER. In addition, its activity can be enhanced by functionalization with noble metals nanoparticles.[9] Unlike in case of HER, accomplishing OER might be more problematic for the metal sulfides due to thermodynamic and kinetic limitations. OER, which is the water oxidation half-reaction, is often considered a bottleneck due to the high overpotential demanded to form the O—O bond.[10] The fact that MoS_2 is quite inert for this reaction due to the too strong metal—sulfur (M—S) bond, seriously limits its application in alkaline electrolyzers.[11] In order to overcome this problem, the number of electrochemical active sites can be increased by incorporating conductive transition metals in the MoS_2 structure, that can act as catalyst for the OER.[12] By hybridizing transition-metal sulfides (CoS_2, NiS_2, FeS_2, and CuS) with highly active MoS_2 nanosheets, a heterostructure catalyst can be achieved, improving largely its bifunctional activity originated from the special interfacial interaction, as well as synergetic catalytic effects.[13] A very good example is the vertically aligned oxygenated–CoS_2–MoS_2 (O–CoMoS) heteronanosheets grown on flexible carbon fiber cloth developed by Sun and coworkers.[14]

M. Guillen-Soler, E. P. Quirós-Díez, J. M. Vila-Fungueiriño, M. del C. Gimenez-Lopez
Centro Singular de Investigación en Química Biológica y Materiales Moleculares (CIQUS)
Universidad de Santiago de Compostela
Santiago de Compostela 15782, Spain
E-mail: maria.gimenez.lopez@usc.es
N. V. Vassilyeva, A. Forment-Aliaga
Instituto de Ciencia Molecular (ICMol)
Universidad de Valencia
C/ Catedrático José Beltrán 2, Paterna, Valencia 46980, Spain
E-mail: alicia.forment@uv.es

The ORCID identification number(s) for the author(s) of this article can be found under https://doi.org/10.1002/adsu.202300607

DOI: 10.1002/adsu.202300607

In this regard, the use of polyoxometalates (POMs), which are a diverse class of anionic metal-oxo clusters constructed mainly by early transition metals in high oxidation states, is very appealing.[15] Moreover, POMs are able to incorporate redox-active metal centers or form hierarchical structures, increasing their potential for electrocatalysis.[15a,16,17] An interesting example of the latest is the synthesis of Pd(II)/POM heterostructure with unique atomic arrangement and high Pd loading, which can be used as highly efficient heterogeneous catalysts, proving the synergistic effect of POM anions and Pd.[18] However, so far, despite the electrocatalytic activity of POMs,[19] their combination with MoS_2 for fast electron kinetics remains rarely explored.

In this study, we report the preparation and functional characterization of an innovative and efficient catalyst for water splitting. This catalyst is created by combining well-known conductive MoS_2 flakes with palladium nanoparticles (PdNPs) and a cobalt-based polyoxometalate, given that cobalt has been demonstrated to be a good transition metal OER catalyst.[19] The hybridization of MoS_2 with POM is facilitated by the involvement of PdNPs, which serve as anchoring points for POM deposition and its unexpected growth into fibers, resulting in the formation of a unique hierarchical heterostructure. The resulting material underwent comprehensive analysis using various chemical and physical techniques. Its activity and stability were assessed through 8-h chronoamperometry experiments and 5000 potential cycles, with the aim of evaluating its potential use in future water splitting devices.

2. Results and Discussion

2.1. Synthesis and Characterization of the Pd/MoS_2

To create a catalytically active POM-Pd-MoS_2 hybrid material, we initially hybridized chemically exfoliated conductive MoS_2 sheets with PdNPs before proceeding with the hybridization involving the $[Na_{11}(H_2O)_{24}H_6][Co_6(H_2O)_2(PW_9O_{34})_2(PW_6O_{26})]\cdot 19H_2O$ POM through metal coordination.[20] The hybridization of MoS_2 with palladium was achieved through the in situ decomposition of $Pd^0{}_2(dba)_3$ (where dba = dibenzylideneacetone) in solution (see Experimental Section). This methodology has been previously reported for the decoration of carbon supports with well-dispersed small PdNPs.[21] It is worth mentioning that the catalytic activation of MoS_2 for HER has been reported through interfacial doping with palladium.[9,22] High-resolution transmission electron microscopy (HRTEM) images shown in Figure S1 (Supporting Information) of the hybrid Pd/MoS_2 demonstrated a good dispersion of small PdNPs, with an average length size of 3.63 ± 0.84 nm (Figure S2, Supporting Information). For this material, no Pd-based crystalline phases were observed even with high-magnification HRTEM images, as can be seen in Figure S1 (Supporting Information). Chemical mapping using energy dispersive X-ray spectroscopy (EDS) in scanning transmission electron microscopy (STEM) further confirmed the presence of palladium homogeneously distributed across the MoS_2 support (Figure S3, Supporting Information). The nanoparticles were mostly immobilized as PdO phase causing no observable changes in morphology of MoS_2 sheets. This was confirmed by X-ray diffraction (XRD) analysis (Figure S4, Supporting Information) showing that the crystalline structure of MoS_2 was preserved, while clear crystalline peaks of Pd metal could not be observed.

As observed in the X-ray photoelectron spectroscopy (XPS) measurements of the Pd/MoS_2 hybrid (Figure S5, Supporting Information), the interaction with the $Pd_2(dba)_3$ complex induced significant oxidation of Mo, resulting in the formation of various oxidation states in Pd. One possible explanation is the intrinsic instability of $Pd_2(dba)_3$ precursor,[21a] which is known to oxidize in presence of water in a MoS_2 suspension, leading to formation of soluble Pd (II) species. Subsequently, Pd (II) is electrostatically absorbed and partially reduced onto the surface of negatively charged 1T-MoS_2. This leads to the oxidation of MoS_2 and the formation of very small PdNPs, surface of which oxidizes upon contact with water. This is in agreement with Pd 3d spectrum (Figure S5, Supporting Information), where the dominant PdO phase at 336.65/342.06 eV with possible contribution of substoichiometric PdO_x constitutes 47% of the sample, whilst reduced metallic Pd (0) is indicated by the doublet of peaks at 335.8/341.15 eV[23] and constitutes of around 35%. Finally, the two peaks at 338.3/343.7 eV corresponding to the area of ≈18% suggest the presence of oxidized Pd (IV) phase, in particular, passivation layer of PdO_2[24] that is usually formed upon exposure to the oxygen of air with possible contribution of $Pd(OH)_4$ hydrated species formed in presence of water.[25]

2.1.1. Synthesis and Characterization of the POM

Prior to incorporating the cobalt-based polyoxometalate into the as-prepared Pd/MoS_2 hybrid, purple crystals of a new sodium-saturated salt of the POM with the formula $[Na_{11}(H_2O)_{24}H_6][Co_6(H_2O)_2(PW_9O_{34})_2(PW_6O_{26})]\cdot 19H_2O$ were isolated (Figures S6–S8, Supporting Information). This was achieved by adding an excess of NaCl followed by slow evaporation of the solvent. The crystal structure was determined using single-crystal X-ray diffraction (Monoclinic, space group $P2_{1/c}$) (see, Table S1, Supporting Information).[26] The observed Co—O and W—O distances in the crystal structure confirm the oxidation states as Co (II) and W (VI), respectively (Figure S9 and Tables S2–S4, Supporting Information). The analyzed structure agrees with the infrared (IR) spectra, where P—O, W=O, and W—O_b vibrations can be clearly identified (Figure S10, Supporting Information). Scanning electron microscopy (SEM) imaging of the POM reflects its crystalline structure and EDX analysis reveals Co:W weight ratio to be 1:14 (Figure S11 and Table S5, Supporting Information). The isolated crystals are highly soluble in water and forming stable bright purple solutions as shown by UV–vis measurements (Figure S12, Supporting Information).

2.1.2. Synthesis and Characterization of the POM/Pd/MoS_2 Hybrid Material

The POM/Pd/MoS_2 hybrid material was prepared by slowly adding a concentrated POM solution to a well-dispersed Pd/MoS_2 suspension and then, isolating it through filtration after several days of stirring. Subsequently, the POM/Pd/MoS_2 hybrid underwent thorough characterization using various techniques. High-magnification HRTEM images show the morphological

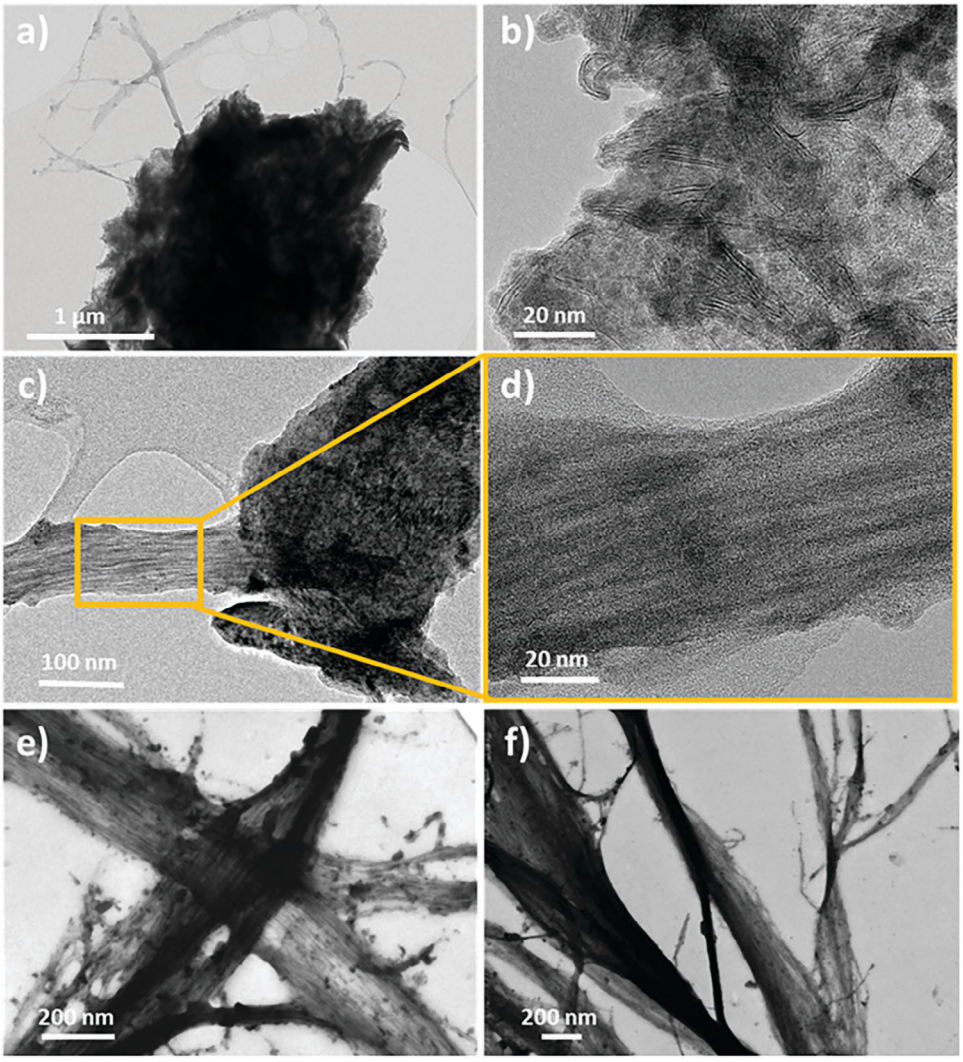

Figure 1. HRTEM images of the POM/Pd/MoS_2 hybrid material showing: a) a general view of the Pd/MoS_2 flakes with POM fibers; b) a region of Pd/MoS_2 flakes; and c,d) closer image of POM fiber growing from Pd/MoS_2 flake. e,f) field-emission SEM images of the POM fibers.

characteristics of the MoS_2 flakes (**Figure 1a**) decorated with small PdNPs (8.16 ± 2.46 nm) (Figure 1b; Figure S13, Supporting Information). However, lower-magnification HRTEM images in Figure 1c reveal that long fibers emanate from the Pd/MoS_2 aggregate, with their origin in the Pd/MoS_2 flakes. These fibers can be observed more closely in the field-emission SEM and HRTEM images in Figure 1c,d. STEM images in Figure 1e,f clearly reveal bundles of long nanofibers. HRTEM demonstrated that these heterostructures polymerize mainly in one direction without strict ordering, as no lattice fringes were appreciated (Figure 1c). EDX analysis of the material confirmed the presence of Mo (37.60% wt.), S (28.86% wt.), Pd (22.26% wt.), Co (1.37% wt.), W (8.74% wt.), and Na (1.17% wt.) (Figure S14 and Table S6, Supporting Information).

STEM-EDX mapping was carried out to elucidate the possible mechanism or the origin of polymerization. As can be seen in **Figures 2** and S15 (Supporting Information), two types of regions can be distinguished: an aggregate region composed mainly by Mo, S, Pd, W, and Co and a filamentous region composed of Co, W, O, and P (and Pd in certain areas). The analysis of Figures 1 and 2 together with the STEM-EDX mapping in Figure S15 (Supporting Information) for all the elements, brings us to the conclusion that POMs were absorbed on the surface of Pd/MoS_2 aggregates giving rise to a polymerization process. Furthermore, a lesser amount of Pd is detected in regions adjacent to the fibers (Figure S16, Supporting Information), indicating its participation in the polymerization process of the POM. This involvement of Pd promotes the extension of longer fibers.

Given that MoS_2 sheets were initially functionalized with Pd, it is expected that Pd would be distributed across the surface of MoS_2 as particles with a Pd (0) core and PdO, PdO_2, and $Pd(OH)_4$ shell (see previous Section 2.1. and Figure S5, Supporting Information). On the other hand, the terminal oxygen atoms of the POMs can serve as anchoring points for noble metal atoms.[27] Therefore, considering the affinity of oxidized Pd species for interactions with metal oxides,[28] one can hypothesize that Pd oxidized species facilitate the attachment of POMs onto PdNPs

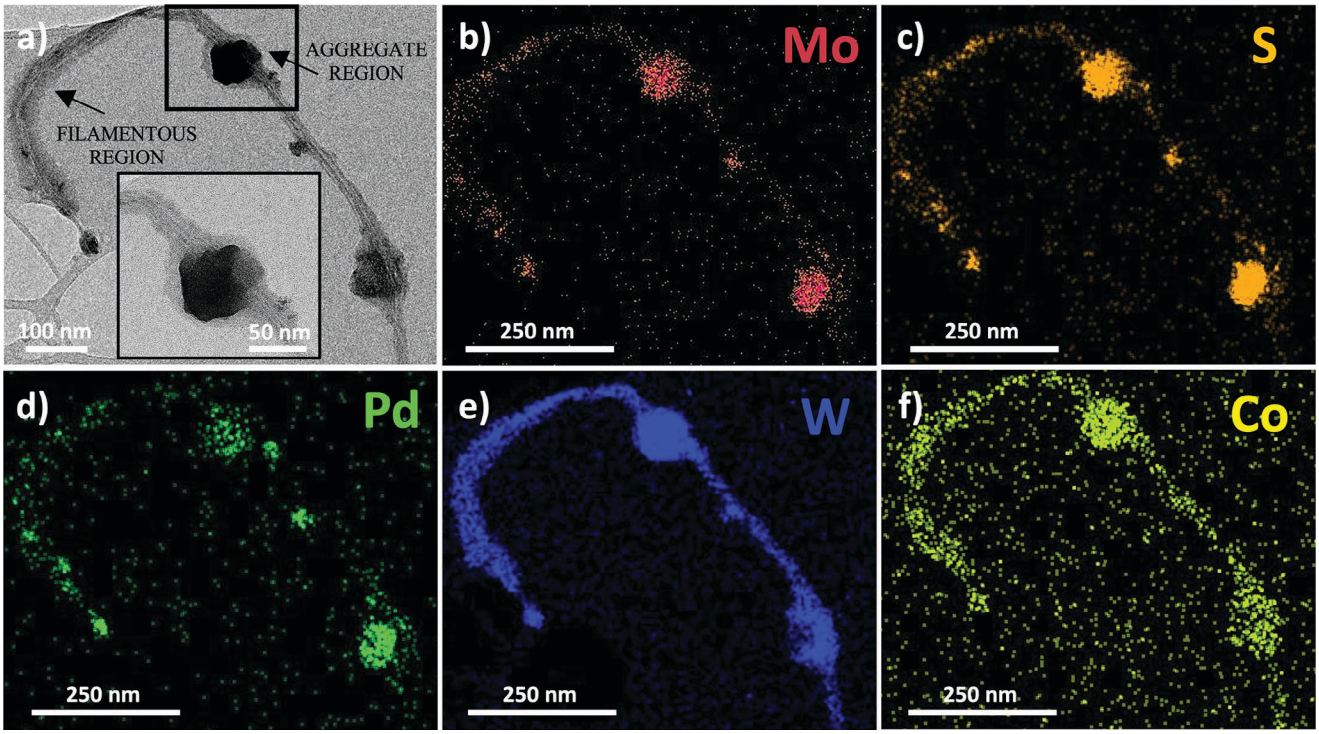

Figure 2. a) HRTEM image of the hybrid POM/Pd/MoS_2 material. Inset shows the zoom of the selected area marked as black square. b–f) STEM-EDX mapping of the HRTEM image is shown in (a).

regions and contribute to further coordination of POMs. Oxide and hydroxide groups can coordinate metallic W, Co, and even non-metallic P cations, leading to the formation of new Pd-O-X bridges (X = W, Co, or P) as the POM polymerizes.[18] Consequently, we propose that the oxidized Pd phase plays a significant role in the formation of POM chains. The presence of soluble Pd (II) species in the solution results in the further extension of POM chains with PdNPs trapped along the fiber-like structures, as depicted in Figure 2 and Figures S15 and S16 (Supporting Information).

Surprisingly, the polymerization develops mainly in one direction, giving rise to filamentous structures where Pd acts as a nucleation point, whereas attaching them to the surface of MoS_2 (**Figure 3**a). This hypothesis is confirmed by STEM-EDX mapping (Figure 3b–f), where the growth of POM fibers (mainly composed by W and Co) originating in PdNPs can be clearly observed. Additionally, polymerization is evident in the EDX spectra taken from various regions of the sample, where the Co:W weight ratio decreases to 1:7 (Table S6, Supporting Information) compared to the ratio found in the pristine POM (Table S5, Supporting Information). This suggests that the polymerization process affects the POM structure, resulting in the loss of W.

Numerous factors, such as pH and time, could influence this process. To establish control over the experiment, we created a material by hybridizing just MoS_2 (without Pd) with POM. In conducting the control experiment, we followed the same synthesis conditions used for POM/Pd/MoS_2 (see Supporting Information). HRTEM images and SEM-EDX mapping (Figures S17 and S18, Supporting Information) indicate the growth of POM particles in the POM/MoS_2 hybrid material, as the POM clusters tend to self-aggregate into rounded shapes due to their weak electrostatic interaction with MoS_2. In contrast to POM/Pd/MoS_2, POM/MoS_2 does not exhibit a fibrous structure, highlighting the key role of the Pd.

These findings confirm our hypothesis about the pivotal role played by PdNPs in attaching the POM clusters for building elongated supramolecular structures. The EDX analysis in Figure S19 and Table S7 (Supporting Information) display low weight percentages of Co, Na, and W present in the sample, implying only minimal interactions with the MoS_2 support to take place without presence of Pd when hybridizing POM with just MoS_2. Therefore, it can be safely concluded, that the observed changes are solely related to intermolecular interactions within Pd-POM-MoS_2, rather than external factors such as solvent or temperature variations.

The XPS spectra shown in **Figure** 4a–d can provide useful information about the chemical state of the POM/Pd/MoS_2 hybrid material. The doublet of peaks at 228.9/232.1 eV emerging in Mo 3d orbit (Figure 4a) corresponds to Mo (IV) state with ≈16% of overall contribution and in this case likely demonstrates coexistence of thermodynamically stable 2H-MoS_2 phase and residual 1T-phase.[29] However, the most prominent phases in the sample after interaction are Mo (V) and Mo (VI) states with possible contribution of substoichiometric oxidized species.[30] In case of Pd 3d scan reflected in Figure 4b, Pd (0), Pd (II), and Pd (IV) oxidation states were detected, indicating no significant difference with bare Pd/MoS_2 structure (Figure S5, Supporting Information). The survey XPS spectra of POM/Pd/MoS_2 hybrid material and the high-resolution C, P, and S XPS spectra are shown in Figure S20 (Supporting Information).

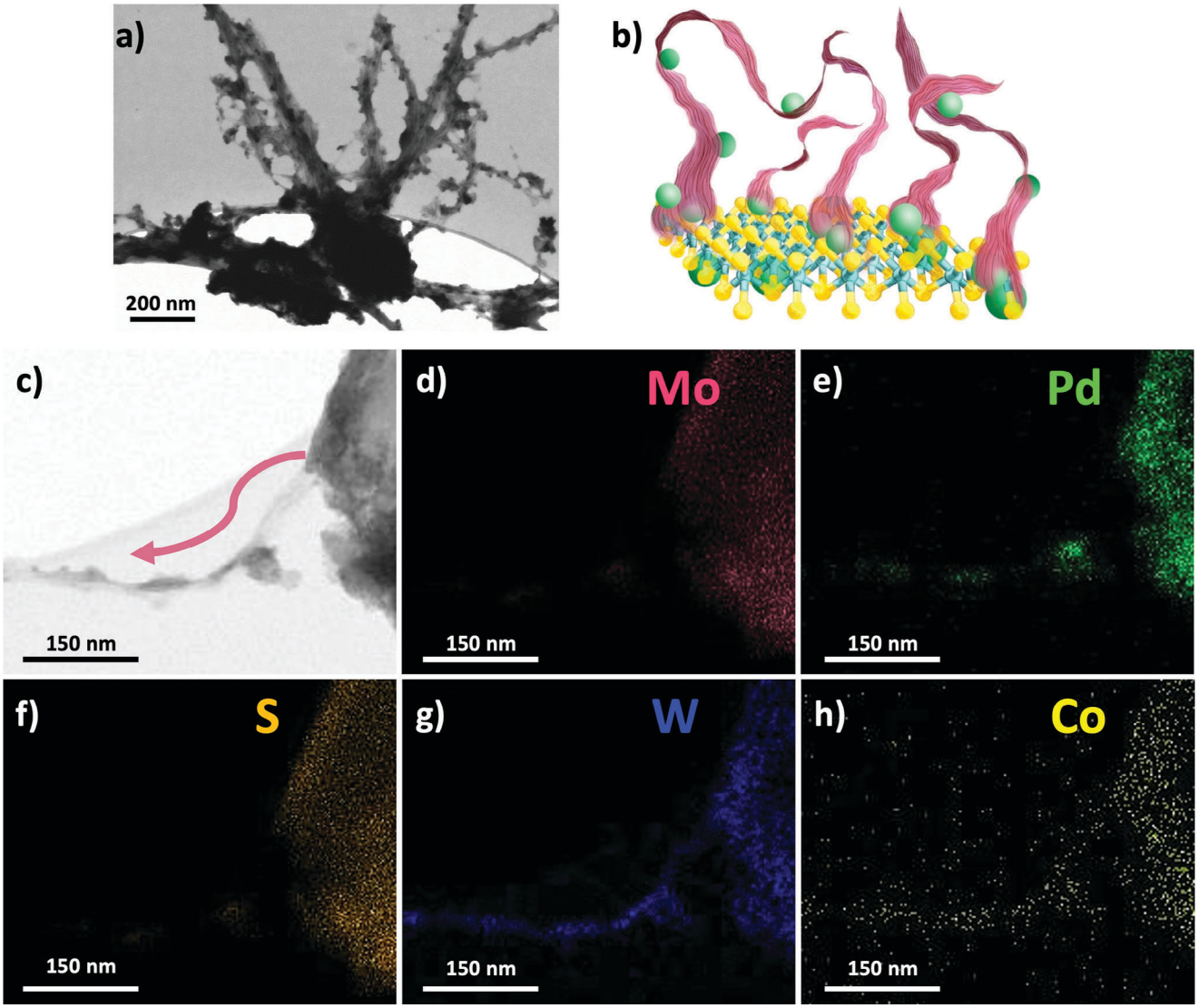

Figure 3. a) Representative field-emission SEM image and b) illustrated figure of POM/Pd/MoS_2. c) STEM-EDX mapping of a region of POM/Pd/MoS_2 where it can be observed the hybridization pathway (marked with a pink arrow) and the growing of the POM fibers.

Regarding the POM fibers of POM/Pd/MoS_2 hybrid material, in W 4f scan (Figure 4c) we observe the two dominant peaks at 35.65/37.75 eV corresponding to the pure W(VI) phase with $5p_{3/2}$ peak of W located in the area around 41 eV.[31] As for Co 2p scan, there is one main chemical state detected (Figure 4d). The main doublet of peaks at 781.6 and 797.5 eV could be attributed to $2p_{3/2}$ and $2p_{1/2}$ states of Co (II), respectively. The spin-orbit splitting of $\Delta = 15.9$ eV clearly suggest that the dominant species is Co (II). Additional evidence for the existence of Co(II) phase is provided by the shake-up lines or satellite peaks located at around 786.6 and 803.4 eV, respectively. The lack of peaks in the area ≈780 eV confirms that no Co(III) phase is present.[32] XPS spectra of POM/MoS_2 structure are displayed in Figure S21 (Supporting Information) for comparison.

Raman spectroscopy using a single 532 nm laser can provide additional information. Thus, Raman spectrum of the POM/Pd/MoS_2 hybrid depicted in Figure 4e was compared with those of POM and chemically exfoliated MoS_2. The bare MoS_2 has the main vibrational modes located at 383 and 409 cm^{-1}, which can be assigned to breathing in-plane $E^1{}_{2g}$ and out-of-plane A_{1g} modes, respectively.[33] The weak band arising at 452 cm^{-1} can be attributed to the longitudinal acoustic phonon mode, whilst two peaks around 481 and 285 cm^{-1} correspond to forbidden A_{2u} and E_{1g} modes, respectively.[34] The three additional vibrational modes exhibited at 155 (J_1), 220 (J_2), and 330 (J_3) cm^{-1} indicate presence of metallic metastable 1T-MoS_2 phase.[35] Furthermore, it has to be highlighted that no band ≈820 cm^{-1}, characteristic for Mo—O—Mo and Mo═O stretch, was detected, therefore, no oxide species of Mo were present in the initial material.[36] The POM displays bands at 820, 970, and 1044 cm^{-1} corresponding to W═O and P—O vibrational modes. The peaks in the region of 100–300 cm^{-1} correspond to O—W—O vibrational modes. In the POM/Pd/MoS_2 hybrid material, both MoS_2 and POM vibrational modes could be distinguished. Unfortunately,

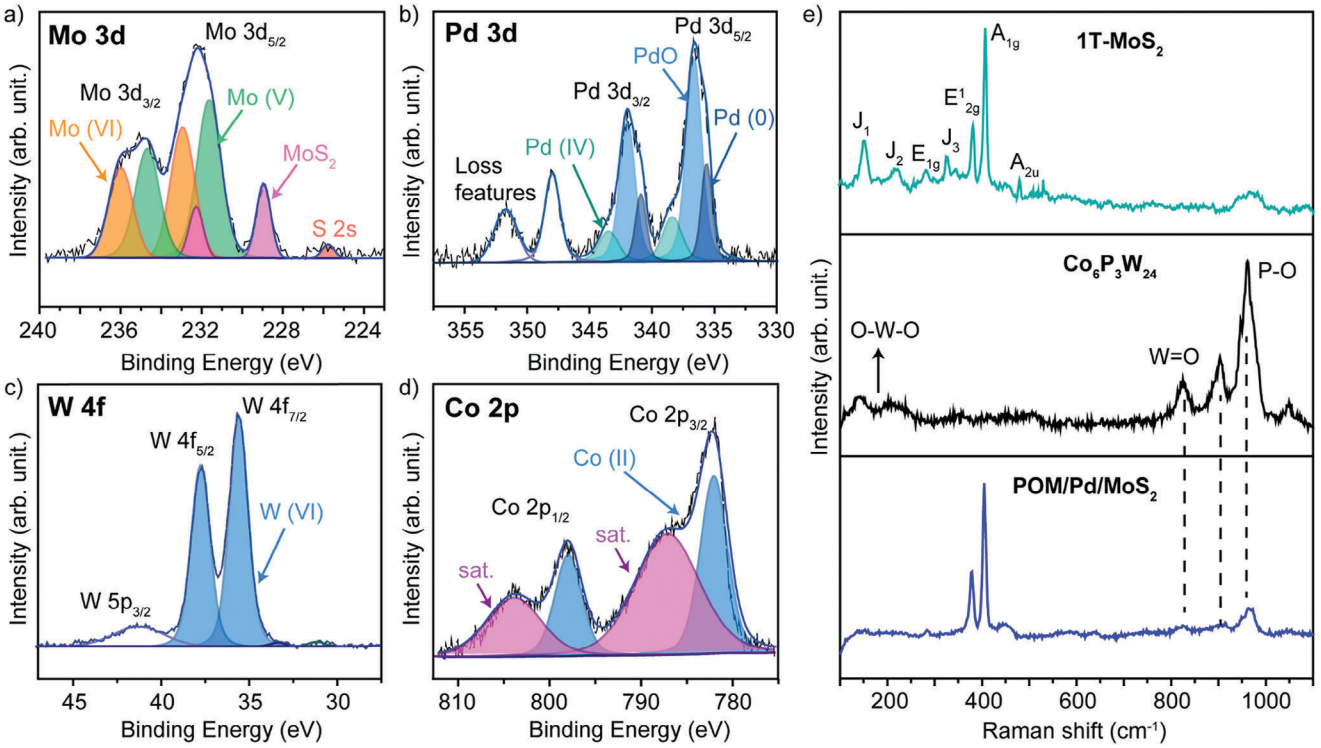

Figure 4. a–d) XPS and e) Raman characterization of POM/Pd/MoS_2 hybrid material.

Mo—O—Mo and Mo═O bands[36] overlap with those corresponding to W═O and P—O vibrational modes, and it is not possible to identify the oxides present on the layers after functionalization.

The aforementioned characterization suggests that the crystalline structure of all constituents has experienced some alterations during the process. The conductive properties of MoS_2 proved crucial for forming a conductive matrix, which effectively facilitated homogenous growth of small-sized PdNPs due to this element's negatively charged surface. Interestingly, only in presence of pre-existing PdNPs, serving as anchoring points, cobalt-based polyoxometalate interacted with MoS_2 and resulted in the formation of elongated supramolecular architectures. This highlights how an intricate interplay among different constituents shapes their properties, yielding a new material with unique features and potential applications in various fields.

2.1.3. Electrochemical Activity and Stability of the POM/Pd/MoS_2 Hybrid

To investigate the electrocatalytic properties of POM/Pd/MoS_2 as bifunctional electrocatalyst, we initially performed HER measurements in 0.5 M H_2SO_4, followed by OER measurements in 0.1 M NaOH using a three-electrode system.[37] For comparison, MoS_2 and the Pd/MoS_2 and POM/MoS_2 hybrids were also measured under the same conditions. Pt/C, Ir/C, and IrO_2/C commercial catalyst were used as benchmark. A graphite rod was used as counter electrode to avoid any possible influence of Pt deposition on the working electrode.

The HER measurements of Pd/MoS_2, compared to that of MoS_2, demonstrated that introduction of PdNPs enhanced the activity, as expected (**Figure 5a**), lowering the potential, required to reach a current density of 10 mA cm^{-2}, from 256 mV in MoS_2 to 131 mV in Pd/MoS_2. On the other hand, when measuring the OER activity of the Pd/MoS_2 material, it exhibited a decrease in activity compared to MoS_2, which was not very significant because of the already intrinsic poor activity of the MoS_2 in catalyzing the OER (Figure 5b).

The overall water splitting activity was achieved after incorporating the POM in the Pd/MoS_2 structure. The resultant hybrid material POM/Pd/MoS_2 exhibited a similar HER activity as Pd/MoS_2, but in exchange the OER activity was enhanced, being comparable to the benchmark catalyst Ir/C and IrO_2/C in alkaline solution (0.1 M NaOH). As shown in Figure 5b, the POM/Pd/MoS_2 heterostructure exhibited an improved OER performance: the obtained values for the onset and the overpotential at 10 mA cm^{-2} are relatively small (1.45 and 0.55 V, respectively) compared to the values obtained when the iridium standard electrocatalyst Ir/C (1.42 and 0.32 V), as well as IrO_2/C (1.35 and 0.45 V) were used under the same electrochemical conditions (Figure 5b).

As control, the POM/MoS_2 material was also tested. It can be concluded that the presence of the POM in the electrode material increments the active sites of the MoS_2 for the OER. However, it is not expected to be a stable material, as discussed above in the characterization section, due to the poor POM-MoS_2 interactions. Besides, it lowered the activity for the HER in comparison with pristine MoS_2.

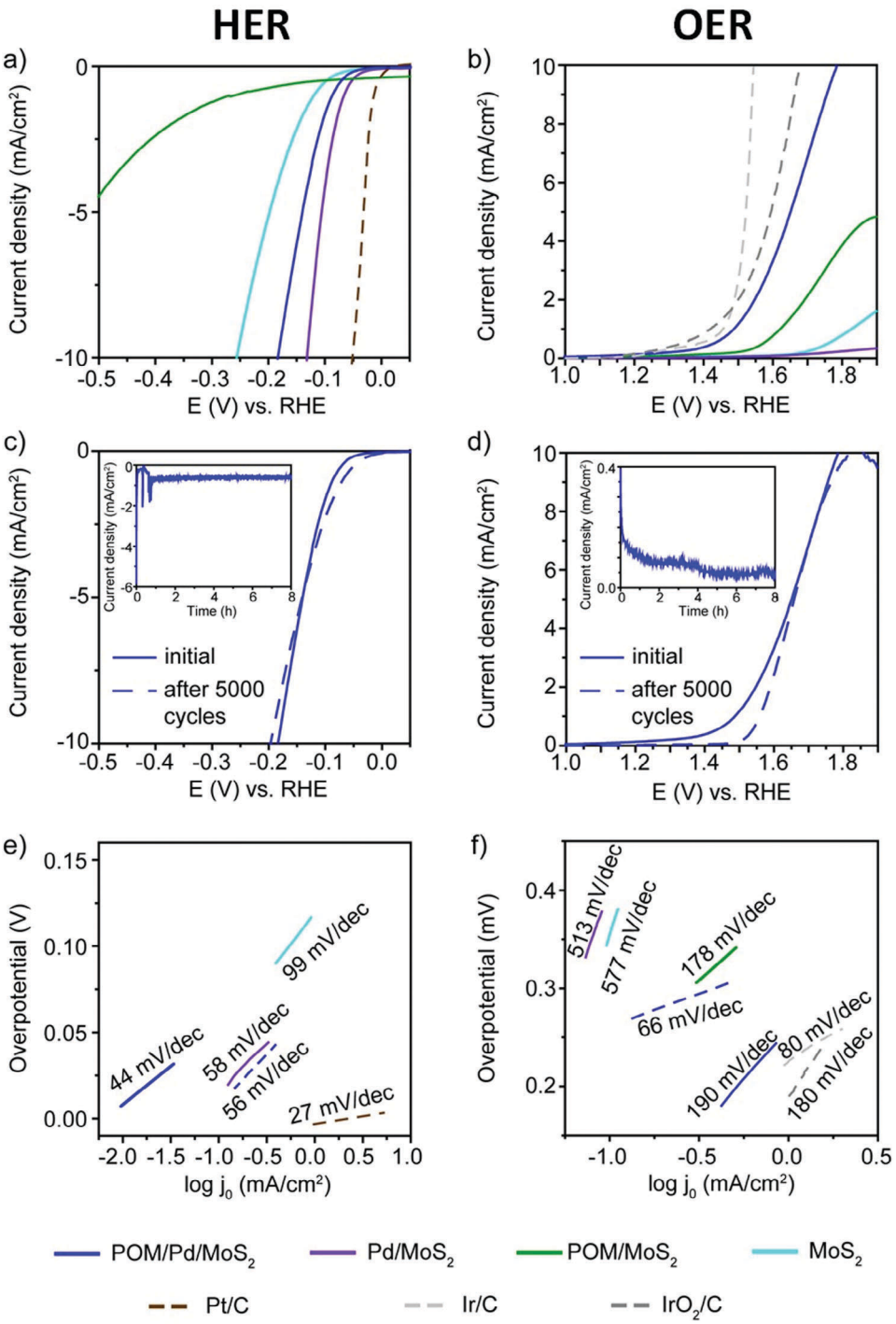

Figure 5. Electrochemical characterization of the as-prepared electrocatalyst materials in this work. a,b) Comparison of the ohmic drop corrected HER (a) and OER (b) polarization curves. c,d) Linear sweep polarization curves for the POM/Pd/MoS_2 electrocatalyst material before and after 5000 potential cycles for the HER (c) and OER (d) activities. Inset figures show an 8 h-CA measurements (see Supporting Information for details). e,f) Tafel plots for the electrocatalyst materials POM/Pd/MoS_2, Pd/MoS_2, and POM/MoS_2 before (solid lines) and after (dashed lines) 5000 potential cycles of the HER and OER (f) compared with the commercial benchmarks (Pt/C, Ir/C, and IrO_2/C).

Therefore, the POM/Pd/MoS_2 presented a better combined HER/OER performance than Pd/MoS_2 based on the linear sweep polarization curves in Figure 5a,b which can be ascribed to the hierarchical POM/Pd/MoS_2 architecture, facilitating electron and mass transport and providing abundant catalytically active sites for OER. The intimate hybridization of POM and Pd/MoS_2 maintains the properties of the two different materials, bringing up the synergistic effect on the active catalytic interface of these heterostructures. The values obtained for OER/HER in POM/Pd/MoS_2 in terms of onset and overpotential are better or comparable to other examples recently reported (Table S8, Supporting Information).

In order to probe the long term-stability of this material for both HER and OER, 8 h-chronoamperometry (CA) measurements were performed and its activity was tested after 5000 potential cycles by continuously applying linear potential sweeps between 0.4 and −0.2 V versus reversible hydrogen electrode (RHE) for HER and between 1.2 and 1.6 V versus RHE for OER at 100 mV s^{-1} scan rate. The POM/Pd/MoS_2 catalyst material remains quite stable after 5000 HER cycles and the 8 h-CA shows no decrease in the current density (Figure 5c). On the other hand, after 5000 OER cycles it exhibited a decrease in activity in terms of the onset (from 0.55 to 1.45 V) and the overpotential (from 1.50 to 1.60 V). The current density maximum observed for the linear scanning voltammetry of POM/Pd/MoS_2 after cycling is due to the oxygen bubble formation in the kinetic region at 1.8 V. During the 8 h-CA, this bubble formation affects the integrity of the electrode, leading to its breakage (Figure S27, Supporting Information), and consequently results in the loss of the electrode material, explaining the observed current density variation with time (Figure 5d). Thus, this result may hold promise for long-term practical applications of the POM/Pd/MoS_2 catalyst after improving the stability of the electrode film.

The Tafel slopes of as-prepared POM/Pd/MoS_2, Pd/MoS_2, and MoS_2 are 44, 58, and 99 mV dec^{-1}, respectively, indicate the favorable HER reaction kinetics for the POM/Pd/MoS_2 (Figure 5e). Moreover, the Nyquist plot displayed in Figure S22 (Supporting Information) obtained from the electrochemical impedance spectroscopy (EIS) revealed that the charge transfer resistance of the POM/Pd/MoS_2 material is lower than that of Pd/MoS_2, POM/MoS_2, and MoS_2 electrodes, demonstrating the faster reaction kinetics and the higher electrical conductivity of POM/Pd/MoS_2. The Tafel slope value after stability test slightly increased from 44 to 56 mV dec^{-1}. For OER kinetics, POM/Pd/MoS_2 initially displayed a large Tafel slope value that after 5000 OER cycles decreased (from 190 to 66 mV dec^{-1}) suggesting a possible change in the mechanism of the reaction due to some rearrangement of the active sites (Figure 5f).

In order to assess the structural changes of the POM/Pd/MoS_2 electrode, XRD, Raman, SEM/EDX, and XPS measurements were conducted after 5000 potential cycles for the HER and OER, respectively, and compared with the measurements done before the stability tests. Complementary XRD and Raman measurements ($\lambda_{ex} = 532$ nm) confirm the presence on the electrode surface of both MoS_2 and POM after OER and HER stability tests (Figure S23, Supporting Information). XPS measurements conducted after 5000 potential cycles for the HER suggest that hydrogen production is primarily promoted by the MoS_2 phase, which is known to be a highly efficient HER catalyst. The most noticeable change after HER is the observed increase in the oxidation peak in the Mo 3d spectrum. This indicates that initial Mo (IV) of MoS_2 undergoes oxidation, leading to the emergence of MoO_3 as the new dominant species (Figure S24, Supporting Information). On the other hand, XPS measurements after 5000 potential cycles for the OER indicate that oxygen production is triggered not only by the POM but also by chemically reactive oxide species of Mo. A significant reduction in the contribution of Mo(VI) is evident, with almost complete recovery of Mo(IV). These changes can be attributed to the emergence of both the thermodynamically stable 2H-MoS_2 phase and MoO_2. It is worth noting that MoO_2 cannot be experimentally distinguished from 2H-MoS_2 by XPS, and its less crystalline structure likely hinders its identification through Raman or XRD.[38] After OER, W (VI) oxide undergoes a significant reduction from WO_3 into W_2O_5, WO_2, and even some metallic W, but no significant changes were observed for the Co peak (Figure S23a, Supporting Information). Pd particles protected with an inert passivating layer, however, remain practically unchanged after OER, as no changes were observed in the XPS spectra (Figure S25, Supporting Information). SEM-EDX confirms the presence of Mo, W, Co, S, and Pd on the electrode surface after both HER and OER stability experiments (Tables S9 and S10 and Figures S26 and S27, Supporting Information).

To confirm and quantify the gas produced, we used an electrochemical cell connected with a Gas-Chromatograph (GC) in a close circuit. The separate detection of H_2 and O_2 with this technique allows us to further confirm the selective production of these gases, as no other peaks are observed in the gas chromatogram. For hydrogen, a total of 6 coulombs were produced in a CA experiment by applying a negative constant current. During this time, the hydrogen peak (at 2.2 min of retention time) was detected in the gas phase after the reaction started. The area of the peak was quantified and compared with the theoretical amount, giving a faradaic efficiency of 83% (Figure S28a,b, Supporting Information). Parallelly, the amount of oxygen detected by a GC matched well with the amount of charge produced during the chronoamperometry experiment. Subsequently, a total of 3.3 coulombs were produced by applying a constant current, hereafter the area of the oxygen peak was monitored and quantified, resulting in an excellent faradaic efficiency of 91% achieved (Figure S28c,d, Supporting Information).

3. Conclusion

In this work, we have reported a straightforward approach for the preparation of a unique hierarchical POM/Pd/MoS_2 heterostructure with great potential as electrocatalyst material for water splitting. Chemically exfoliated MoS_2 provided a conductive matrix for the formation of the composite and its negative surface charge played a key role in the homogeneous growth of PdNPs with small average size. Afterward, the interaction between cobalt-based polyoxometalate and MoS_2 is triggered due to presence of PdNPs, that serve as anchoring points for POM deposition and the formation of elongated fibers. The as-prepared POM/Pd/MoS_2 hybrid material showed high activity and stability, performing similarly to previously activated MoS_2 for the HER and demonstrating significantly improved OER activity, comparable to benchmark catalysts Ir/C and IrO_2/C

in alkaline environments. This was achieved through assembly of POM (OER catalyst), PdNPs (HER catalyst), and conductive matrix provided by MoS_2 flakes, resulting in the synergistic effect of these electroactive constituents. Our approach introduces a novel strategy for designing cost-effective and highly efficient alkaline electrolyzers.

4. Experimental Section

Materials and Methods: Crystalline powder of molybdenum (IV) sulfide and *n*-butyllithium solution (1.6 M in hexane) were purchased from Alfa Aesar and Sigma–Aldrich, respectively. Iridium Oxide (IrO_2) was purchased from Sigma–Aldrich. Iridium (20%) on Vulcan XC-72 (Ir/C) was purchased from Premeter co. Platinum, nominally 20% on carbon black (Pt/C), HISPEC 3000 was purchased from Alfa Aesar. All other reagents and solvents were purchased from Sigma–Aldrich (Spain) and used without any further purification.

IR spectra were measured using a Bruker Alpha FTIR spectrometer with a platinum ATR module. SEM and EDX analysis were performed on a ZEISS EVO LS 15 with EDX module (Oxford Inca x-act with 129 eV of resolution and WD 8.5). HRTEM was performed on a JEOL JEM F200 microscope equipped with a cold field-emission gun (Cold-FEG) operated at 200 kV with an ultra-high-resolution pole piece. TEM images were acquired using a Gatan OneView camera. EDS was performed with a Centurio Large Angle Silicon Drift Detector (SDD) that collects X-rays from a detection area of 100 mm^2. Copper grids were used for HR-TEM measurements. The Raman spectra were performed with RENISHAW Raman microscope with laser Ion Ar (514 nm). Single-crystal XRD was measured on a Bruker D8 Venture Photon 100 CMOS κ–geometry diffractometer system equipped with an Incoatec high brillance IμS microsource (MoKα, $\lambda = 0.71073$ Å) and an Incoatec HeliosTM multilayer optics monochromator. XPS analysis of the samples was performed using a Thermo Scientific K-Alpha ESCA/XPS instrument equipped with aluminum Kα monochromatized radiation at 1486.6 eV X-ray source. To guarantee a homogeneous surface conductivity, a charge compensation (electron flood gun) gun was used to minimize surface charging. Surface charge compensation was performed by using both a low-energy flood gun (electrons in the range of 0–14 eV) and a low-energy Argon ions gun. The XPS measurements were carried out using monochromatic Al-Ka radiation ($h\nu = 1486.6$ eV). Photoelectrons were collected from a take-off angle of 90° relative to the sample surface. The measurement was done in a constant analyzer energy mode with a 100 eV pass energy for survey spectra and 30 eV pass energy for high-resolution spectra. Surface elemental composition was determined using the standard Scofield photoemission cross-sections. Binding energies were determined using the C 1s peak at 284.8 eV as a charge reference. The CasaXPS software was used to analyze the high-resolution spectra. The background was fitted through a Shirley-type function.

Synthesis of POM: In a 50 mL round-bottom flask, 4 g of $Na_2WO_4{\cdot}2H_2O$ (12.12 mmol, 9 equiv.) and 190 mg of Na_2HPO_4 (1.34 mmol, 1 equiv.) were dissolved in 11 mL of water. Then, the *pH* of the reaction was adjusted to seven with a solution of HCl 6 M. After that, 779 mg of $Co(NO_3)_2{\cdot}6H_2O$ (2.68 mmol, 2 equiv.) was added to the mixture and let the reaction heating at 100 °C for 2 h. During this time, the purple suspension was dissolved. Excess of NaCl was added to the hot mixture and immediately filtered off under vacuum. The filtrate was left under air to obtain purple crystals of the compound with the formula $[Na_{11}(H_2O)_{24}H_6][Co_6(H_2O)_2(PW_9O_{34})_2(PW_6O_{26})]{\cdot}19H_2O$ (150 mg) suitable for single-crystal XRD measurements.

Chemical Exfoliation of MoS_2: To obtain a suspension of MoS_2 flakes a previously reported strategy of chemical exfoliation via solvothermal treatment using *n*-BuLi intercalation protocol was employed.[39] First, Teflon autoclave was loaded with bulk MoS_2 crystals (2.0 mmol, 320.0 mg) and then *n*-BuLi 1.6 M solution in hexane was added (5 mL, 8 mmol). The procedure was carried out inside a nitrogen-filled glovebox. Once sealed, the autoclave was heated up to 100 °C for 2 h. After the heating treatment Li-intercalated MoS_2 crystals were filtered and washed with hexane inside the glovebox to remove unreacted residues. The collected black powder was then dispersed in 10 mL of cool degassed Milli-Q water. The dispersion was then bath-sonicated for 1 h and dialyzed overnight. The resulting suspension was bath-sonicated for 30 min and then centrifuged at 800 rpm for 30 min to separate unexfoliated bulk crystals. Finally, the obtained aqueous suspension of MoS_2 flakes was used without additional purification.

Synthesis of Pd/MoS_2: A MoS_2 solution (3.2 mg mL^{-1}) was placed into a round bottom flask and degassed with Argon. A solution of $Pd_2(dba)_3$ (8.24 mg) in dry THF (10 mL) was then slowly added to the MoS_2 suspension under vigorous stirring. The mixture was further stirred for 2 days at 40 °C. The Pd/MoS_2 was then separated by centrifugation (five times at 7500 rpm for 8 min) and washed repeatedly with acetone. The obtained solid was dried overnight at 50 °C.

Synthesis of POM/Pd/MoS_2: The POM (100 mg) were dissolved in 2.5 mL of ionized water and added dropwise under sonication to a suspension of Pd/MoS_2 (2 mg mL^{-1} in water, *pH* 6, previously sonicated for 30 min). The mixture was stirred at room temperature for 3 days, and then, filtered through a hydrophilic PTFE membrane, and washed repeatedly and copiously with water to collect a black solid (20 mg).

Synthesis of POM/MoS_2: The POM (100 mg) were dissolved in 2.5 mL of ionized water and added dropwise under vigorous stirring to a 2.5 mL of MoS_2 solution (3.2 mg mL^{-1} in water, *pH* 5.6). The mixture was stirred at room temperature for 3 days. The POM/MoS_2 material was then separated by centrifugation (five times at 7500 rpm for 8 min) and washed with water to obtain a black solid.

Film Electrode Preparation: To prepare the working electrode, a dispersion of 5 mg of each of the samples in 1 mL of isopropanol was used as an ink. Thereafter, 20 μL of the obtained homogeneous catalyst ink was dropped onto a mirror polished glassy carbon electrode (0.196 cm^2 of geometric surface area) being the final mass loading 0.51 mg cm^{-2}. Then, 20 μL of Nafion (5 wt.%) was added and the electrode was dried under ambient conditions.

Electrochemical Measurements: An Autolab potentiostat PGSTAT302N was used to measure the electrocatalytic activities toward HER and OER. All the electrochemical measurements were conducted in a three-electrode set-up, with a glassy carbon electrode (GCE), RHE, and a carbon rod as working, reference and counter electrode, respectively. Cyclic voltammetry measurements under N_2 and O_2-saturated electrolyte were performed to characterize the catalysts before electrochemical measurements. Linear scanning voltammetry (LSV) was conducted in an O_2-saturated 0.1 M NaOH aqueous solution to study OER activity at a scanning rate of 5 mV s^{-1}. Stability tests were carried out by potential sweeping (1.4 to 1.75 V) during 5000 OER cycles at a rate of 100 mV s^{-1}. To study HER, LSV were conducted in a H_2-saturated 0.5 M H_2SO_4 aqueous solution between 0.2 V and −0.8 V at a scanning rate of 5 mV s^{-1}. Stability tests were carried out by potential sweeping (0.2 to −0.4 V) during 5000 HER cycles at a rate of 100 mV s^{-1}. 8 h-CA experiments were carried by applying either a negative (−0.2 V) or a positive (1.5 V) constant current for the HER and the OER, respectively. For OER, the electrolyte was saturated previously with oxygen, and the material was compared with the commercial Iridium on carbon (Ir/C), whereas for HER the material was compared with the commercial Platinum on carbon (Pt/C) under the same conditions.

Single-Crystal X-Ray Diffraction Measurements: A clear violet, prism-like specimen of POM, approximate dimensions 0.020 mm x 0.020 mm x 0.070 mm, was used for the X-ray crystallographic analysis. The X-ray intensity data were measured on a Bruker D8 VENTURE PHOTON-III C14 κ-geometry diffractometer system equipped with a Incoatec IμS 3.0 microfocus sealed tube (Mo Kα, $\lambda = 0.71073$ Å) and a multilayer mirror monochromator. A total of 5312 frames were collected. The total exposure time was 11.00 h. The frames were integrated with the Bruker SAINT software package using a narrow-frame algorithm. The integration of the data using a monoclinic unit cell yielded a total of 1 068 436 reflections to a maximum θ angle of 31.57° (0.68 Å resolution), of which 45 453 were independent (average redundancy 23.506, completeness = 99.8%, R_{int} = 13.71%, R_{sig} = 4.63%) and 30 335 (66.74%) were greater than $2\sigma(F^2)$. The final cell constants of a = 17.4706(10) Å, b = 22.3110(12) Å, c = 35.059(2) Å, β = 95.960(2)°, volume = 13 591.7(13) $Å^3$, were based upon the refinement of the XYZ-

centroids of 9102 reflections above 20 σ(I) with 4.672° < 2θ < 62.53°. Data were corrected for absorption effects using the Multi-Scan method (SADABS). The ratio of minimum to maximum apparent transmission was 0.710. The calculated minimum and maximum transmission coefficients (based on crystal size) were 0.3190 and 0.6770. The structure was solved and refined using the Bruker SHELXTL Software Package, using the space group $P2_{1/c}1$, with $Z = 2$ for the formula unit, $Co_{12}Na_{22}O_{304}P_6W_{48}$. The final anisotropic full-matrix least-squares refinement on F^2 with 1522 variables converged at R1 = 4.63%, for the observed data and wR2 = 12.84% for all data. The goodness-of-fit was 1.074. The largest peak in the final difference electron density synthesis was 5.877 e^- Å^{-3} and the largest hole was −3.687 e^- Å^{-3} with an RMS deviation of 0.501 e^- Å^{-3}. On the basis of the final model, the calculated density was 3.687 g cm^{-3} and F(000), 13 280 e^-. Deposited on Cambridge Database: CCDC 2 280 064.

Supporting Information

Supporting Information is available from the Wiley Online Library or from the author.

Acknowledgements

M.G.-S., N.V.V., and E.P.Q.-D. contributed equally to the work. This work has received financial support from the Ministry of Science of Spain (RYC-2016-20258, PID2021-127341OB-I00, TED2021-131451BC21 and PDC2022-133925-I00 for M.d.C.G.-L. and IJC2020-044369-I for J.M.V.-F.), the European Research Council (ERC) [Starting Grant (NANOCOMP-679124) and ZABCAT (966743) for M.d.C.G.-L.], the Generalitat Valenciana (MFA/2022/050 for A.F. and fellowship GRISOLIAP/2019/030 for N.V.), the Xunta de Galicia (Centro singular de investigación de Galicia accreditation 2019–2022, ED431G 2019/03 and ED481A-2020/155), and the European Union (European Regional Development Fund—ERDF).

Conflict of Interest

The authors declare no conflict of interest.

Data Availability Statement

The data that support the findings of this study are available in the supplementary material of this article.

Keywords

bifunctional electrocatalyst, heterostructures, molybdenum disulfide, palladium, polyoxometalate, water splitting

Received: November 30, 2023
Published online:

[1] a) S. Huang, Y. Meng, S. He, A. Goswami, Q. Wu, J. Li, S. Tong, T. Asefa, M. Wu, *Adv. Funct. Mater.* **2017**, *27*, 1606585; b) Y. Tan, P. Liu, L. Chen, W. Cong, Y. Ito, J. Han, X. Guo, Z. Tang, T. Fujita, A. Hirata, M. W. Chen, *Adv. Mater.* **2014**, *26*, 8023.

[2] X. Jia, Y. Zhao, G. Chen, L. Shang, R. Shi, X. Kang, G. I. N. Waterhouse, L.-Z. Wu, C.-H. Tung, T. Zhang, *Adv. Energy Mater.* **2016**, *6*, 1502585.

[3] J.-S. Li, Y. Wang, C.-H. Liu, S.-L. Li, Y.-G. Wang, L.-Z. Dong, Z.-H. Dai, Y.-F. Li, Y.-Q. Lan, *Nat. Commun.* **2016**, *7*, 11204.

[4] a) P. Jiang, Q. Liu, Y. Liang, J. Tian, A. M. Asiri, X. Sun, *Angew. Chem., Int. Ed.* **2014**, *53*, 12855; b) J. Tian, Q. Liu, A. M. Asiri, X. Sun, *J. Am. Chem. Soc.* **2014**, *136*, 7587; c) J. Hou, Y. Sun, S. Cao, Y. Wu, H. Chen, L. Sun, *ACS Appl. Mater. Interfaces* **2017**, *9*, 24600; d) X. F. Lu, L. Yu, X. W. (D.). Lou, *Sci. Adv.* **2019**, *5*, eaav6009.

[5] a) R. Xu, R. Wu, Y. Shi, J. Zhang, B. Zhang, *Nano Energy* **2016**, *24*, 103; b) L. Fang, W. Li, Y. Guan, Y. Feng, H. Zhang, S. Wang, Y. Wang, *Adv. Funct. Mater.* **2017**, *27*, 1701008; c) B. Liu, Y.-F. Zhao, H.-Q. Peng, Z.-Y. Zhang, C.-K. Sit, M.-F. Yuen, T.-R. Zhang, C.-S. Lee, W.-J. Zhang, *Adv. Mater.* **2017**, *29*, 1606521.

[6] a) T. A. Shifa, F. Wang, K. Liu, K. Xu, Z. Wang, X. Zhan, C. Jiang, J. He, *Small* **2016**, *12*, 3802; b) H. Li, P. Wen, Q. Li, C. Dun, J. Xing, C. Lu, S. Adhikari, L. Jiang, D. L. Carroll, S. M. Geyer, *Adv. Energy Mater.* **2017**, *7*, 1700513; c) Z.-H. Xue, H. Su, Q.-Y. Yu, B. Zhang, H.-H. Wang, X.-H. Li, J.-S. Chen, *Adv. Energy Mater.* **2017**, *7*, 1602355.

[7] a) J.-X. Feng, S.-H. Ye, H. Xu, Y.-X. Tong, G.-R. Li, *Adv. Mater.* **2016**, *28*, 4698; b) X.-F. Lu, L.-F. Gu, J.-W. Wang, J.-X. Wu, P.-Q. Liao, G.-R. Li, *Adv. Mater.* **2017**, *29*, 1604437; c) W. Liu, H. Liu, L. Dang, H. Zhang, X. Wu, B. Yang, Z. Li, X. Zhang, L. Lei, S. Jin, *Adv. Funct. Mater.* **2017**, *27*, 1603904; d) K. Jin, H. Seo, T. Hayashi, M. Balamurugan, D. Jeong, Y. K. Go, J. S. Hong, K. H. Cho, H. Kakizaki, N. Bonnet-Mercier, M. G. Kim, S. H. Kim, R. Nakamura, K. T. Nam, *J. Am. Chem. Soc.* **2017**, *139*, 2277; e) J.-X. Feng, H. Xu, Y.-T. Dong, S.-H. Ye, Y.-X. Tong, G.-R. Li, *Angew. Chem., Int. Ed.* **2016**, *55*, 3694; f) M. Martin-Sabi, J. Soriano-López, R. S. Winter, J.-J. Chen, L. Vilà-Nadal, D.-L. Long, J. R. Galán-Mascarós, L. Cronin, *Nat. Catal.* **2018**, *1*, 208; g) Q. Shi, C. Zhu, D. Du, Y. Lin, *Chem. Soc. Rev.* **2019**, *48*, 3181.

[8] a) Y. Liu, C. Xiao, M. Lyu, Y. Lin, W. Cai, P. Huang, W. Tong, Y. Zou, Y. Xie, *Angew. Chem., Int. Ed.* **2015**, *54*, 11231; b) L.-L. Feng, G. Yu, Y. Wu, G.-D. Li, H. Li, Y. Sun, T. Asefa, W. Chen, X. Zou, *J. Am. Chem. Soc.* **2015**, *137*, 14023; c) M. Kuang, P. Han, Q. Wang, J. Li, G. Zheng, *Adv. Funct. Mater.* **2016**, *26*, 8555; d) Y. Sun, F. Alimohammadi, D. Zhang, G. Guo, *Nano Lett.* **2017**, *17*, 1963.

[9] Z. Luo, Y. Ouyang, H. Zhang, M. Xiao, J. Ge, Z. Jiang, J. Wang, D. Tang, X. Cao, C. Liu, W. Xing, *Nat. Commun.* **2018**, *9*, 2120.

[10] a) A. Grimaud, A. Demortière, M. Saubanère, W. Dachraoui, M. Duchamp, M.-L. Doublet, J.-M. Tarascon, *Nat. Energy* **2016**, *2*, 16189; b) J.-J. Duan, R.-L. Zhang, J.-J. Feng, L. Zhang, Q.-L. Zhang, A.-J. Wang, *J. Colloid Interface Sci.* **2021**, *581*, 774.

[11] a) G. Hai, H. Gao, G. Zhao, W. Dong, X. Huang, Y. Li, G. Wang, *iScience* **2019**, *20*, 481; b) W. Chen, Y. Liu, Y. Li, J. Sun, Y. Qiu, C. Liu, G. Zhou, Y. Cui, *Nano Lett.* **2016**, *16*, 7588; c) H. L. Chia, C. C. Mayorga-Martinez, Z. Sofer, P. Lazar, R. D. Webster, M. Pumera, *Adv. Funct. Mater.* **2021**, *31*, 2009083.

[12] X. Mu, Y. Zhu, X. Gu, S. Dai, Q. Mao, L. Bao, W. Li, S. Liu, J. Bao, S. Mu, *J. Energy Chem.* **2021**, *62*, 546.

[13] Q. Sun, Y. Tong, P. Chen, B. Zhou, X. Dong, *ACS Sustainable Chem. Eng.* **2021**, *9*, 4206.

[14] J. Hou, B. Zhang, Z. Li, S. Cao, Y. Sun, Y. Wu, Z. Gao, L. Sun, *ACS Catal.* **2018**, *8*, 4612.

[15] a) D. Gao, I. Trentin, L. Schwiedrzik, L. González, C. Streb, *Molecules* **2020**, *25*, 157; b) M. Anjass, G. A. Lowe, C. Streb, *Angew. Chem., Int. Ed.* **2021**, *60*, 7522.

[16] F. M. B. Gusmão, D. Mladenovic, K. Radinovic, D. M. F. Santos, B. Sljukic, *Energies* **2022**, *15*, 9021.

[17] a) Y. Han, J. Lan, K. Li, L. Yang, C. Zhu, J. Chen, *Chem. - Asian J.* **2022**, *17*, e202200950; b) S. Wang, Z. Sun, C. Zhang, L. Ni, C. Wang, Y. Gao, L. Lv, J. Chang, W. Hao, *Inorg. Chem. Commun.* **2014**, *41*, 47.

[18] J. Hou, L. Zhang, Y. Li, Y. Xia, Z. Huang, H. Fu, P. Guo, Y. Ao, *Inorg. Chem. Front.* **2021**, *8*, 1528.

[19] a) D. Zang, Y. Huang, Q. Li, Y. Tang, Y. Wei, *Appl. Catal., B* **2019**, *249*, 163. b) J. Gautam, Y. Liu, J. Gu, Z. Ma, J. Zha, B. Dahal, L.-N. Zhang, A. N. Chishti, L. Ni, G. Diao, Y. Wei, *Adv. Funct. Mater.* **2021**, *31*, 2106147. c) Z. Zeb, Y. Huang, L. Chen, W. Zhou, M. Liao, Y. Jiang, H. Li, L. Wang, L. Wang, H. Wang, T. Wei, D. Zang, Z. Fan, Y. Wei, *Coord. Chem. Rev.* **2023**, *482*, 215058.

[20] I. Ullah, A. Munir, A. Haider, N. Ullah, I. Hussain, *Nanophotonics* **2021**, *10*, 1595.
[21] a) S. S. Zalesskiy, V. P. Ananikov, *Organometallics* **2012**, *31*, 2302; b) M. Aygün, M. Guillen-Soler, J. M. Vila-Fungueiriño, A. Kurtoglu, T. W. Chamberlain, A. N. Khlobystov, M. Del Carmen Gimenez-Lopez, *ChemSusChem* **2021**, *14*, 4973.
[22] L. G. Bach, M. L. N. Thi, Q. B. Bui, H.-T. Nhac-Vu, *Synth. Met.* **2019**, *254*, 172.
[23] P. Wu, Y. Huang, L. Kang, M. Wu, Y. Wang, *Sci. Rep.* **2015**, *5*, 14173.
[24] I. A. Chetyrin, A. V. Bukhtiyarov, I. P. Prosvirin, A. K. Khudorozhkov, V. I. Bukhtiyarov, *Top. Catal.* **2020**, *63*, 66.
[25] a) L. P. A. Guerrero-Ortega, E. Ramírez-Meneses, R. Cabrera-Sierra, L. M. Palacios-Romero, K. Philippot, C. R. Santiago-Ramírez, L. Lartundo-Rojas, A. Manzo-Robledo, *J. Mater. Sci.* **2019**, *54*, 13694; b) R. Rahul, R. K. Singh, B. Bera, R. Devivaraprasad, M. Neergat, *Phys. Chem. Chem. Phys.* **2015**, *17*, 15146; c) T. L. Barr, *J. Phys. Chem.* **1978**, *82*, 1801.
[26] W. Wu, T. Teng, X.-Y. Wu, X. Dui, L. Zhang, J. Xiong, L. Wu, C.-Z. Lu, *Catal. Commun.* **2015**, *64*, 44.
[27] T. Hirano, K. Uehara, K. Kamata, N. Mizuno, *J. Am. Chem. Soc.* **2012**, *134*, 6425.
[28] A. L. Luna, D. Dragoe, K. Wang, P. Beaunier, E. Kowalska, B. Ohtani, D. Bahena Uribe, M. A. Valenzuela, H. Remita, C. Colbeau-Justin, *J. Phys. Chem. C* **2017**, *121*, 14302.
[29] Z. Liu, Z. Gao, Y. Liu, M. Xia, R. Wang, N. Li, *ACS Appl. Mater. Interfaces* **2017**, *9*, 25291.
[30] F. Werfel, E. Minni, *J. Phys. C: Solid State Phys.* **1983**, *16*, 6091.
[31] N. Minh Vuong, D. Kim, H. Kim, *Sci. Rep.* **2015**, *5*, 11040.
[32] T. Zhou, Z. Cao, H. Wang, Z. Gao, L. Li, H. Ma, Y. Zhao, *RSC Adv.* **2017**, *7*, 22818.
[33] F. Güller, A. M. Llois, J. Goniakowski, C. Noguera, *Phys. Rev. B* **2015**, *91*, 075407.
[34] J.-U. Lee, K. Kim, S. Han, G. H. Ryu, Z. Lee, H. Cheong, *ACS Nano* **2016**, *10*, 1948.
[35] N. H. Attanayake, A. C. Thenuwara, A. Patra, Y. V. Aulin, T. M. Tran, H. Chakraborty, E. Borguet, M. L. Klein, J. P. Perdew, D. R. Strongin, *ACS Energy Lett.* **2018**, *3*, 7.
[36] S. Kothaplamoottil Sivan, A. K. K. Padinjareveetil, V. V. T. Padil, R. Pilankatta, B. George, C. Senan, M. Cerník, R. S. Varma, *Clean Technol. Environ. Policy* **2019**, *21*, 1549.
[37] a) I. Amorim, J. Xu, N. Zhang, Z. Yu, A. Araújo, F. Bento, L. Liu, *Chem. Eng. J.* **2021**, *420*, 130454; b) J. Luo, D. A. Vermaas, D. Bi, A. Hagfeldt, W. A. Smith, M. Grätzel, *Adv. Energy Mater.* **2016**, *6*, 1600100; c) D. A. Vermaas, S. Wiegman, T. Nagaki, W. A. Smith, *Sustainable Energy Fuels* **2018**, *2*, 2006.
[38] J. Yan, A. Rath, H. Wang, S. H. Yu, S. J. Pennycook, D. H. C. Chua, *Mater. Res. Lett.* **2019**, *7*, 275.
[39] a) L. Zhou, B. He, Y. Yang, Y. He, *RSC Adv.* **2014**, *4*, 32570; b) M. Morant-Giner, R. Sanchis-Gual, J. Romero, A. Alberola, L. García-Cruz, S. Agouram, M. Galbiati, N. M. Padial, J. C. Waerenborgh, C. Martí-Gastaldo, S. Tatay, A. Forment-Aliaga, E. Coronado, *Adv. Funct. Mater.* **2018**, *28*, 1706125.